metals

MDPI

Article

Texture and Lattice Strain Evolution during Tensile Loading of Mg–Zn Alloys Measured by Synchrotron Diffraction

Xiaohua Zhou [1], Changwan Ha [2], Sangbong Yi [2], Jan Bohlen [2], Norbert Schell [3], Yuanqing Chi [4], Mingyi Zheng [4] and Heinz-Günter Brokmeier [1,2,*]

1 Institute of Materials Science and Engineering, Clausthal University of Technology, Agricolastrasse 6, D-38678 Clausthal-Zellerfeld, Germany; xz09@tu-clausthal.de
2 Magnesium Innovation Centre, Helmholtz-Zentrum Geesthacht, Max-Planck-Str 1, D-21502 Geesthacht, Germany; changwan.ha@hzg.de (C.H.); sangbong.yi@hzg.de (S.Y.); jan.bohlen@hzg.de (J.B.)
3 Helmholtz-Zentrum Geesthacht, GEMS outstation at DESY, Notkestraße 85, D-22607 Hamburg, Germany; norbert.schell@hzg.de
4 School of Materials Science and Engineering, Harbin Institute of Technology, Harbin 150001, China; chiyuanqing29@163.com (Y.C.); zhenghe@hit.edu.cn (M.Z.)
* Correspondence: heinz-guenter.brokmeier@tu-clausthal.de; Tel.: +49-(0)-5323-72-2867

Received: 29 November 2019; Accepted: 10 January 2020; Published: 15 January 2020

Abstract: To explore the effect of neodymium (Nd) on the deformation mechanisms of Mg–Zn alloys, texture and lattice strain developments of hot-rolled Mg–Zn (Z1) and Mg–Zn–Nd (ZN10) alloys were investigated using in situ synchrotron diffraction and compared with elasto-viscoplastic self-consistent simulation under tensile loading. The Nd-containing ZN10 alloys show much weaker texture after hot rolling than the Nd-free Z1 alloy. To investigate the influence of the initial texture on the texture and lattice strain evolution, the tensile tests were carried out in the rolling and transverse direction. During tension, the {002}<100> texture components develop fast in Z1, which was not seen for ZN10. On the other hand, <100> fiber // loading direction (LD) developed in both alloys, although it was faster in ZN10 than in Z1. Lattice strain investigation showed that <101> // LD-oriented grains experienced plastic deformation first during tension, which can be related to basal slip activity. This was more apparent for ZN10 than for Z1. The simulation results show that the prismatic slip plays a vital role in the plastic deformation of Z1 directly from the beginning. In contrast, ZN10 plastic deformation starts with dominant basal slip but during deformation prismatic slip becomes increasingly important.

Keywords: texture; lattice strain; synchrotron diffraction; elasto-viscoplastic self-consistent simulation (EVPSC); Mg-Nd-Zn

1. Introduction

Magnesium (Mg) and its alloys have been manufactured in large quantities for the automobile industry and as aeronautic and 3C products [1] due to its low density of 1.74 g/cm^3. However, the pronounced plastic anisotropy has limited the wide applications of Mg and its alloys in the automotive industry [2–9]. The reason of anisotropy is the hcp crystal structure, which shows limited available activated dislocation system at room temperature. The most common deformation modes include basal slip, prismatic slip, pyramidal slip, and tension twinning. To overcome this anisotropy problem, one must modify the microstructure to have less preferred orientation, optimized grain size, and balanced nano-defects. Many researchers have investigated the effect of texture [10–12], grain size [5,11,13,14], precipitation [15–18], and solutes [19–21] on the deformation behavior of Mg

alloys. Bohlen et al. [8] discussed the benefits regarding ductility and potential formability of the addition of rare-earth elements (REs) into Mg alloys. The addition of yttrium (Y) to Mg has been proposed to improve ductility because of increasing activation of <c + a> slip mode [19,21], increase the critical resolved shear stress (CRSS) for basal slip, <c + a> slip and {10.2} twinning comparing pure Mg and other common alloys [19–21]. Compared to Y, fewer studies have been performed on the influence of neodymium (Nd) on deformation. Herrera-Solaz et al. [22] reported the effect of Nd on the isotropic mechanical behavior of Mg-Mn alloys. On one hand, they found the higher CRSS ratio of basal slip modes and twinning ($CRSS_{basal}/CRSS_{twinning}$) for Mg-Mn alloy than for pure Mg and on the other hand the lower $CRSS_{non\text{-}basal}/CRSS_{twinning}$ ratio for Mg-Mn alloy than for pure Mg. Zhang et al. [23] investigated the extended and stabilized dislocation configuration and the improved ductility due to the decrease stacking fault energy with the addition of REs (in [23] REs = Pr, Nd, Gd, Tb, Dy) using density functional theory. Most studies focused on the effect of addition of REs in pure Mg. Ha et al. [24] discussed the influence of Nd and Ca addition on the dislocation activity and texture changes of Mg–Zn alloys. They found the high activation of prismatic <a> slip and pyramidal <c + a> slip was due to the addition of Nd or Ca into the Mg–Zn alloys. Nevertheless, the influence of REs especially Nd on the deformation mechanism of Mg–Zn binary alloy system is still unclear.

The aim of the present study is to obtain understanding of the effect of Nd to Mg–Zn alloy during tensile deformation. To achieve this goal, the texture and lattice strain evolution were measured using in situ measurements at synchrotron diffraction, which were compared with elasto-viscoplastic self-consistent simulation to describe in more detail the activation of each glide system. Mg–Zn system was chosen as base material due to the similar texture as pure Mg and their attractive practical applications as a degradable biomaterial [25].

2. Experimental and Simulation Procedure

2.1. Materials

Two different Mg alloys, ZN10 (Mg-1.0Zn-0.7Nd wt. %) and Z1 (Mg-1Zn wt. %), were prepared for the present study, while a very small amount of Zirconium (0.13% Zr) is used in Z1 as a grain refiner in order to avoid abnormal grain growth during rolling and annealing [8,26]. Rectangular slabs were machined to the dimensions of 100 mm × 200 mm × 20 mm for the rolling experiments. Before rolling, the Z1 and ZN10 billets were homogenized at 400 °C for 20 h and at 500 °C for 18 h, respectively. The rolling procedure consisted of different passes with different thickness reduction degrees, each referring to a true strain,

$$\varphi = -\ln(h_{m+1}/h_m) \quad (1)$$

where m is the number of the pass and h_m is the sample thickness after pass m. The two alloys were hot-rolled at 400 °C. Z1 alloy was primarily rolled with the two passes at $\varphi = 0.1$, subsequently rolled with two passes at $\varphi = 0.15$, then finally rolled with the two passes at $\varphi = 0.2$. For ZN10 alloy, it was rolled with three passes at $\varphi = 0.1$, then four passes at $\varphi = 0.15$. After each rolling pass, the sheets were reheated at 400 °C for 15 min to keep the rolling temperature constant. The rolled sheets, with a thickness of 8.0 ± 0.1 mm, were air cooled. Finally, the rolled sheets were annealed at 400 °C for 15 min (Z1) and 30 min (ZN10) to produce a similar grain size.

The microstructure of the sheets were examined by optical microscopy after using standard metallographic sample preparation and etching by a picric acid-based etchant [27]. The average grain size was determined by computer-aided linear intercept measurements based on the micrographs from longitudinal sections.

2.2. In Situ Synchrotron Diffraction during Tensile Testing

Standard cylindrical tensile samples (DIN 50125) with 4 mm in diameter and 20 mm in gauge length were machined along the rolling direction (RD) and the transverse direction (TD), respectively. In situ tensile tests were carried out at room temperature (RT) with an initial strain rate of 1.5×10^{-4} s^{-1}

with a Universal Testing Machine (UTM) mounted at the High Energy Materials Science (HEMS) Beamline at PETRA III P07B (DESY, Hamburg, Germany). Figure 1 shows the beamline with the (UTM) setup.

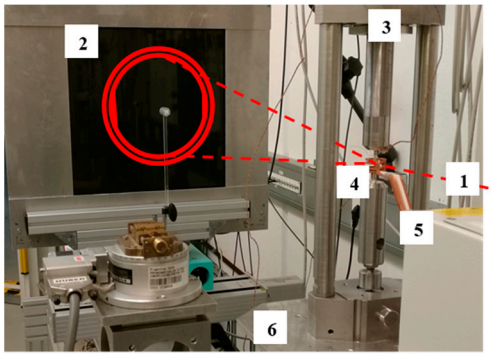

1: Incoming hard X-ray beam
2: Area detector
3: UTM
4: Sample
5: Inductor
6: Rotation stage

Figure 1. Beamline setup for texture measurement at HEMS P07B. Incoming hard X-ray and diffracted beam is marked with red line and circles.

The texture measurements were carried out at nominal strains of 0%, 2%, 5%, 10%, 15% and 20%. The tensile tests were stopped (but not unloaded) for pole figure measurements at these points. Texture measuring time at each nominal strain was approximately 8 min. For pole figure measurements, the sample rotation was used in 3° steps for 180° before loading and for 105° during loading, respectively. In addition, the sample was continuously exposed during rotation every 3° for 3 s, to obtain great grain statistics. The beam with a wavelength of 0.14235 Å and beam size of 0.6 mm × 0.6 mm was used. The sample to detector distance was 1409 mm, calibrated by LaB_6 standard powder. Complete Debye–Scherrer rings were collected with an image plate area detector type Perkin Elmer XRD 1622 (PerkinElmer Technologies GmbH & Co. KG; Walluf, Germany, Type: XRD 1621 CN3-EHS, Serial No.: 723-10194). Data evaluations for pole figures were taken from Debye–Scherrer rings including background subtraction using programs FIT2D and SABO (inhaus software). The orientation distribution functions (ODFs) were calculated using the iterative series expansion method with positivity correction based on the set of six pole figures (10.0), (00.2), (10.1), (11.0), (10.2) and (10.3) [28]. The volume fractions of each texture component were estimated by ideal components and ideal fibers using MTEX. MTEX is a free Matlab toolbox for representing, analyzing and interpreting crystallographic textures, based on pole figure or EBSD measurements. MTEX can import, analyse and visualize diffraction pole figure data, to calculate an orientation density function (ODF), to compute pole figure or ODF characteristics, to model ODF in terms of model functions, to simulate pole figure, to write or change scripts for multiple use, and others. MTEX is a versatile free and open-source software toolbox for texture analysis and modeling [29].

In addition to the texture measurements, the lattice strain evolution was measured during the tensile deformation of the samples. The diffraction patterns were continuously collected at every 8 s without pausing the load. Due to the high speed of data collection one can follow the lattice strain behavior along the complete stress-strain curve. Line position and line broadening are very sensitive to the elastic and plastic behavior of the material. The focus in this study was on the lattice strain evolution as function of the strain calculated by

$$\varepsilon = \frac{d_{hkl} - d_{0,hkl}}{d_{0,hkl}} \quad (2)$$

where $d_{0,hkl}$ refers to the lattice spacing at initial condition. To determine the lattice spacing d_{hkl} parallel to the loading direction (LD) a ± 5° segment was integrated from complete Debye–Scherrer rings.

2.3. Modeling Procedure

The elasto-viscoplastic self-consistent (EVPSC) model is applied to simulate the texture and mechanical behavior during the tensile deformation. The EVPSC model was originally developed by Molinari et al. [30] and was recently implemented by Wang et al. [31] to be applicable to large strain and to arbitrary crystal structure. The detailed description of the model is available in elsewhere [32] [19,33–39].

The plastic deformation of a crystal is attributed to slip and twinning modes, in terms of which the grain level plastic strain rate $\dot{\varepsilon}_p$ is computed following the equation:

$$\dot{\varepsilon}_p = \sum_{\alpha} \dot{\gamma}^{\alpha} P^{\alpha} \tag{3}$$

where $\dot{\gamma}^{\alpha}$ and P^{α} are shear rate and Schmid tensor of slip/twining system α, respectively. For Mg alloys, four deformation mechanisms, including {00.2}<11.0> basal slip, {10.0}<11.0> prismatic slip, {11.2}<11.3> pyramidal <c + a> slip and {10.2}<10.1> tensile twinning, are generally considered in the plasticity modeling. For both slip and twinning modes, the shear rate is expressed by a rate-sensitive relation [40]:

$$\dot{\gamma}^{\alpha} = \dot{\gamma}_0 \left|\tau^{\alpha}/\tau^{\alpha}_{cr}\right|^{\frac{1}{m}} sgn(\tau^{\alpha}) \tag{4}$$

where $\dot{\gamma}_0$ is the reference shear rate, τ^{α} is the resolved shear stress, τ^{α}_{cr} is the CRSS and m is the strain rate sensitivity. In particular, the polar nature of twin activation should be considered, namely if the resolved shear stress is along the anti-twinning direction, the corresponding twinning system will not be activated.

In the EVPSC model, the evolution of CRSS τ^{α}_{cr} is considered following an empirical extended Voce hardening rule:

$$\dot{\tau}^{\alpha}_{cr} = \frac{d\hat{\tau}^{\alpha}}{d\Gamma} \sum_{\beta} h^{\alpha\beta} \left|\dot{\gamma}^{\beta}\right| \tag{5}$$

where $\Gamma = \sum_{\alpha} \int \left|\dot{\gamma}^{\alpha}\right| dt$ is the accumulated shear strain in the grain, and $h^{\alpha\beta}$ is the latent hardening coupling coefficient which empirically determines the obstacles of system β on system α. The threshold stress $\hat{\tau}^{\alpha}$ is determined by:

$$\hat{\tau}^{\alpha} = \tau^{\alpha}_0 + \left(\tau^{\alpha}_1 + \theta^{\alpha}_1 \Gamma\right)\left(1 - \exp\left(-\frac{\theta^{\alpha}_0 \Gamma}{\tau^{\alpha}_1}\right)\right) \tag{6}$$

τ^{α}_0 is the initial CRSS, θ^{α}_0 and θ^{α}_1 correspond to the initial and terminal strain hardening rates respectively, and τ^{α}_1 is the back-extrapolated flow stress.

The orientation of every grain with anisotropic property contributes to the texture characteristic of the material. The measured initial texture was simplified by MTEX selecting 2000 orientations (φ1, Φ, φ2) and was used as the input texture for the EVPSC modeling. The macroscopic loading conditions are acting on the grain level with a self-consistent manner by deformation. The main fitting parameters for these models are CRSS values of the chosen slip systems and/or twinning to balance between measured and simulated stress-strain curve.

3. Results

3.1. Microstructure and Texture at the Rolled State

The optical micrographs of the initial sheets are presented in Figure 2. It shows recrystallized microstructures without twins for both alloys. The average grain sizes of Z1 and ZN10 are comparable at 27 μm and 23 μm, respectively (Figure 2).

The initial textures examined by synchrotron X-ray diffraction are presented by the recalculated (10.0) and (00.2) pole figures and the inverse pole figure in RD, Figure 3 (Z1) and Figure 4 (ZN10).

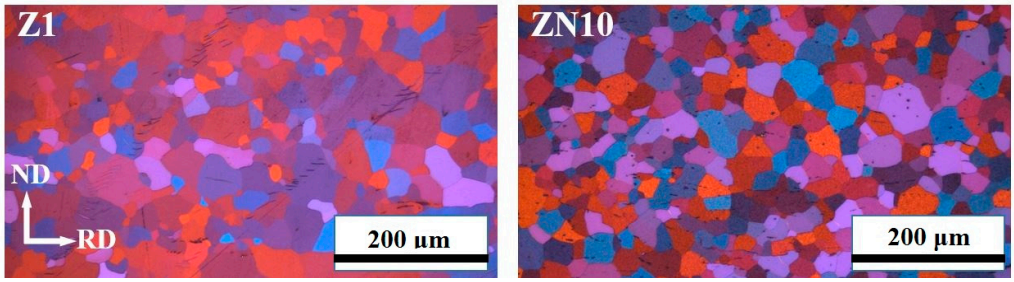

Figure 2. Optical micrographs of the annealed Z1 and ZN10.

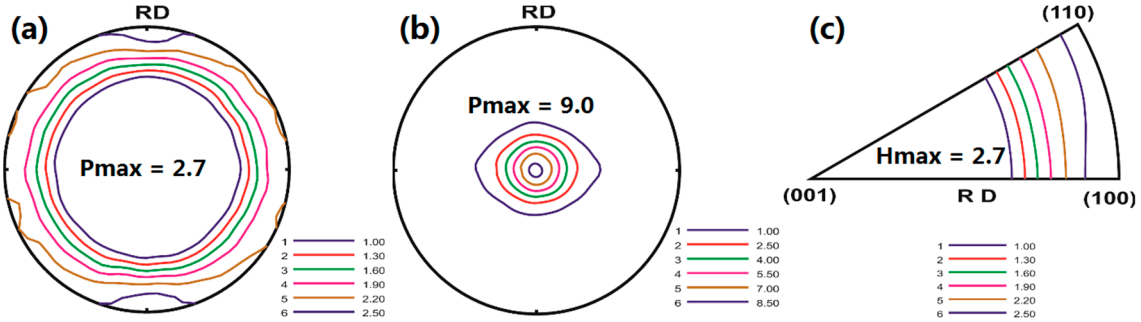

Figure 3. The initial pole figure of Z1: (**a**) (10.0) pole figure; (**b**) (00.2) pole figure; (**c**) the inverse pole figure in RD.

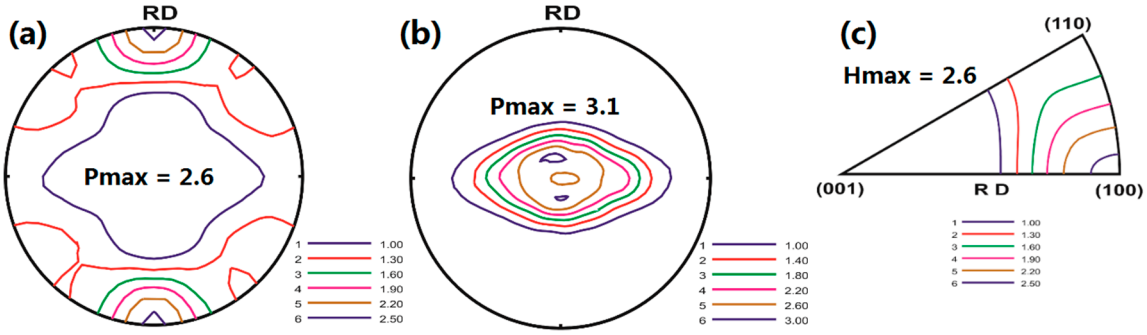

Figure 4. The initial pole figure of ZN10: (**a**) (10.0) pole figure; (**b**) (00.2) pole figure; (**c**) the inverse pole figure in RD.

Z1 has the typical rolling texture, i.e., <00.2> fiber // normal direction (ND), where many grains have orientation with c-axis parallel to ND with a spread of approximately 35°. The texture sharpness is P_{max} = 9.0 mrd (mrd = multiple of random distribution). A second much weaker texture component is a partial <10.0> fiber // RD, seen by the higher intensity in RD-direction of the (10.0) pole figure as well as in the spread of ±45° in TD direction in the (00.2) pole figure. The inverse pole figure expresses an intermediate state, where the material is on this way from ideal deformation texture (<10.0> // RD) to ideal recrystallization texture (<11.0> // RD).

ZN10 shows a much weaker texture (P_{max} = 3.1 mrd) than Z1, which is related on one hand to a higher spread of some texture components and on the other to the development of weaker texture. There is lower importance of the ideal <00.2> fiber // ND and the higher spread of the partial <10.0> fiber // RD with ±75°. The ratio of the orientation spread // ND is ±40° to RD/±75° to TD. Moreover, (00.2)<10.0> ideal component is seen in ZN10 but not in Z1. The inverse pole figure does not show such a strong movement from the (10.0) corner to the (11.0) corner, which indicates less recrystallization of ZN10 than Z1. This may be related to the Nd-content. Moreover, the in-plane anisotropy of ZN10 is higher than in Z1.

3.2. Mechanical Properties

Figure 5 shows the true stress–true strain curves of Z1 and ZN10 along RD and TD at RT.

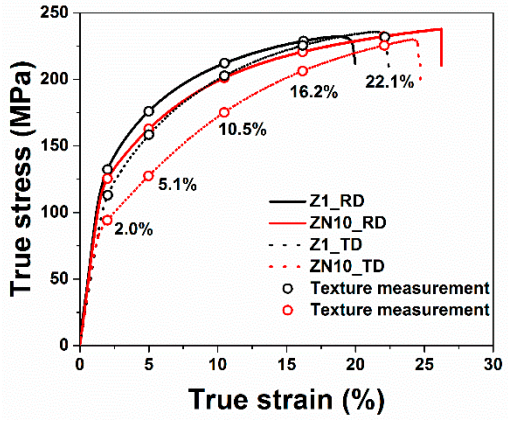

Figure 5. True stress- strain curves of Z1 and ZN10 along RD and TD.

ZN10 shows a stronger RD/TD anisotropy in yield tensile strength (YS) and ultimate tensile strength (UTS) than Z1. While the UTS has values between 181 MPa and 195 MPa, similar in both alloys, the YS is higher in Z1 (123 MPa // RD) than in ZN10 (84 MPa // TD). Elongation is higher in ZN10 than in Z1. The tensile properties are listed in Table 1.

Table 1. Tensile properties along RD and TD (YS: yield strength in MPa, UTS: ultimate tensile strength in MPa, ε_{UTS}: uniform elongation in %, ε_F: fracture elongation in %).

Alloys	Sample Direction	YS	UTS	ε_{UTS}	ε_F
Z1	RD	123	195	16	22
	TD	105	192	18	25
ZN10	RD	115	188	17	>30
	TD	84	181	27	28

The in-plane anisotropy can be explained by the orientation spread given in chapter 3.1 and by comparing (the inverse pole figures: IPF) IPF_{RD} with IPF_{TD}. Figure 6 shows IPF of Z1 and ZN10. It can see clearly that ZN10 shows much higher variation between RD and TD which indicates differences in the properties in both directions.

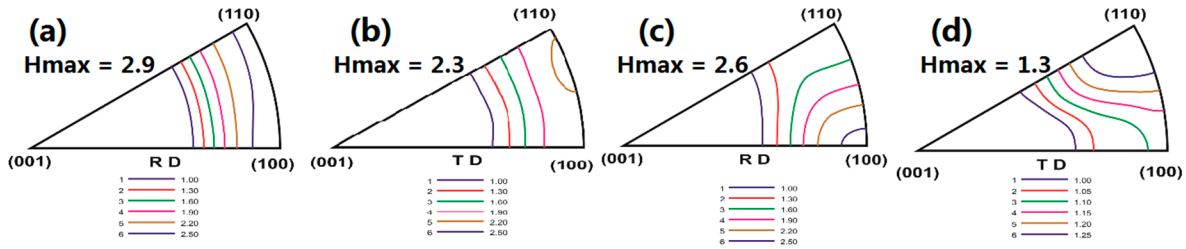

Figure 6. Inverse pole figures of alloys: (**a**) Z1 in RD; (**b**) Z1 in TD; (**c**) ZN10 in RD; (**d**) ZN10 in TD.

3.3. Texture Evolution during in situ Tensile Test

Texture evolution of Z1 and ZN10 during tension in the RD is presented in Figure 7. The quantitative fractions of texture components (Figure 8) were analyzed by MTEX to describe the texture development [29]. Three texture components, <00.2> fiber // ND, <10.0> fiber // RD and {00.2}<10.0> component, were found for both alloys after deformation. These three texture components with 10° angle of texture components are used for simulation by MTEX.

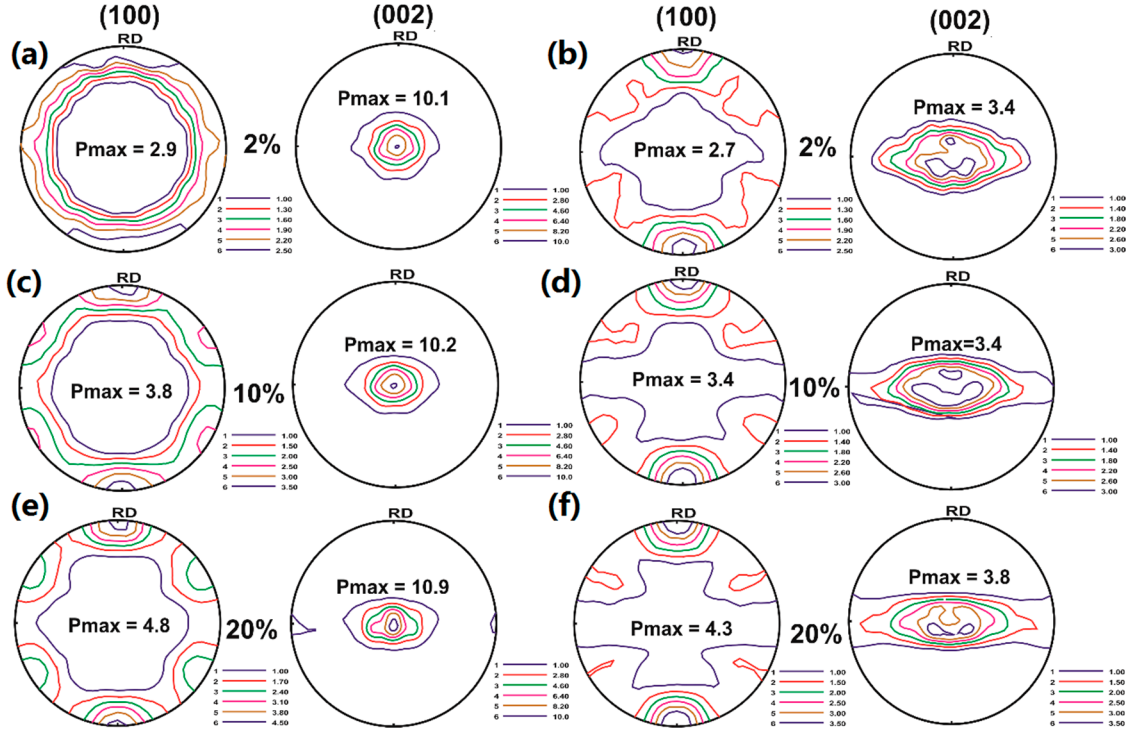

Figure 7. Texture development during tension along RD at different strain: (**a**) Z1 at 2%; (**b**) ZN10 at 2%; (**c**) Z1 at 10%; (**d**) ZN10 at 10%; (**e**) Z1 at 20%; (**f**) ZN10 at 20%.

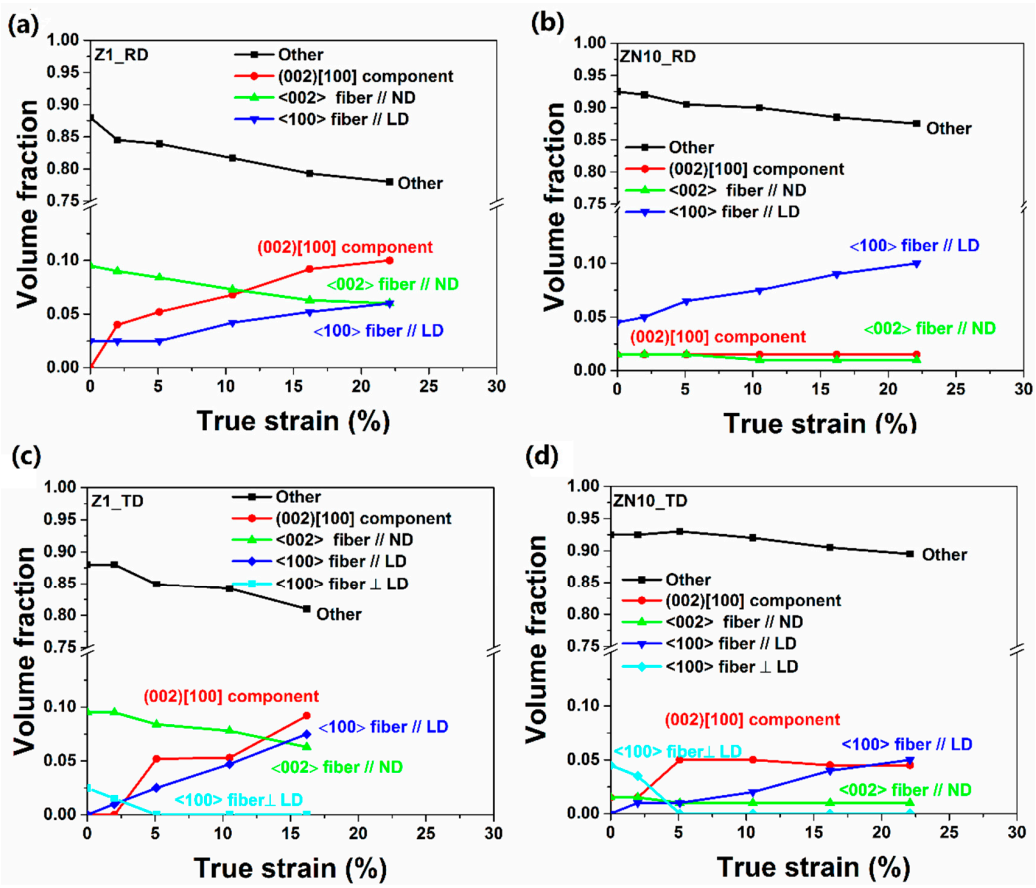

Figure 8. Volume fraction of texture components: (**a**) Z1 in RD; (**b**) ZN10 in RD; (**c**) Z1 in TD; (**d**) ZN10 in TD.

Z1 along RD:

During the following deformation, the max pole density of pole figures of (10.0) and (00.2) planes gradually increased from P_{max} = 2.9 mrd and 10.1 mrd at 2% strain to P_{max} = 4.8 mrd and 10.9 mrd at 20% strain. The broadening of basal poles from ND toward TD and RD showed no significant difference, <10.0> partial fiber // RD did not become a complete fiber. However, the volume fraction of {00.2}<10.0> component increased during the tensile testing. When the strain reached 20%, new texture component could be observed from TD in the (00.2) pole figure. The fraction of texture components at the initial condition (Figures 3 and 8), is 2.5% for <10.0> partial fiber // LD which is parallel to LD, 9.5% for <00.2> fiber // ND which perpendicular to LD and the remaining components. The fraction of <00.2> fiber // ND is decreasing during tension from 9.5% to 5%. Partial <10.0> fiber//RD is increasing from 2.5% without strain to about 5.5% at the largest strain during tension. The {00.2}<10.0> component is new and grows with higher load.

ZN10 along RD:

The intensity of (10.0) and (00.2) planes increased from 2.7 mrd and 3.4 mrd at 2% strain to 4.3 mrd and 3.8 mrd at 20% strain during tension. The basal plane spread from ND toward TD during tension and tilted ±20° to TD. The broadening from ND toward TD reached ±90° at 10% strain, i.e., the texture components <100> partial fiber // RD comes to <100> fiber // RD. The texture component <00.2> fiber // ND reduced to partial fiber when the tensile strain was larger than 10%, while no obvious change was visible for the {002}<100> component during the tensile test. The fraction of texture components for tensile tests along RD (Figure 8b) at the initial condition (Figure 4) is 1.5% for {00.2}<100> component and <00.2> fiber // ND, 4.5% for <10.0> partial fiber // LD. It is to mention that the fractions of <00.2> fiber // ND and {002}<100> component remained stable at around 1.5% during the tensile test. The value of <10.0> partial fiber // RD increased from 4.5% at without strain to 9.5% at largest strain.

In the case of tensile tests along TD, at 2% strain the texture of Z1 did not change compared to the initial textures, but in ZN10, a <100> fiber // LD is visible at 2% strain but not in Z1, the intensity of (100) and (002) planes gradually decreased from Pmax = 2.4 mrd and 3.4 mrd at the starting condition to Pmax = 1.8 mrd and 3.0 mrd at 2% strain for ZN10 alloy. The texture components <100> partial fiber // RD reduced. During the following deformation, the intensity of (100) and (002) planes gradually increased for the Z1 alloy. In ZN10, the intensity of (002) is stable, but intensity of (100) increased. In Z1, the tendency of texture evolution is very similar to the RD sample. In case of ZN10, the broadening from ND toward TD is shortening, and the broadening from ND to RD increased but did not reach ±90° until fracture, i.e., the texture components <100> partial fiber//TD grows but does not come to <100> fiber // TD. The texture components <100> partial fiber // RD is not visible from 10% strain. The texture component <002> fiber // ND reduced to partial fiber at 20% strain.

The quantitative fractions of texture components are shown in Figure 8c,d. The tendency of TD samples are similar compared RD sample in Z1, i.e., in Z1, {002}<100> component and <100> fiber // LD increase, <002> fiber // ND decreases and <100> fiber ⊥ LD disappeared during tension. In ZN10, {002}<100> component and <002> fiber // ND are stable during plastic deformation, the fraction of {002}<100> component and random are higher up to large strain in TD than in RD. <100> fiber ⊥ LD disappeared, <100> fiber // LD increases during whole tensile test, but slower than the RD sample.

3.4. Lattice Strain Evolution during in Situ Measurements

The lattice strain evolutions of different {hkl} lattice planes in parallel to the LD are shown in Figure 9. The intensities of some {hkl} peaks are too low to get accurate peak positions, e.g., {002} in LD. Therefore, four {hkl} planes {100}, {101}, {110} and {201} were analyzed in this study. It can be seen that the lattice strain curve of different {hkl} planes showed different behavior, such as different 'yield point' of lattice stain—true strain curve and different hardening rate, i.e., some planes deform easier.

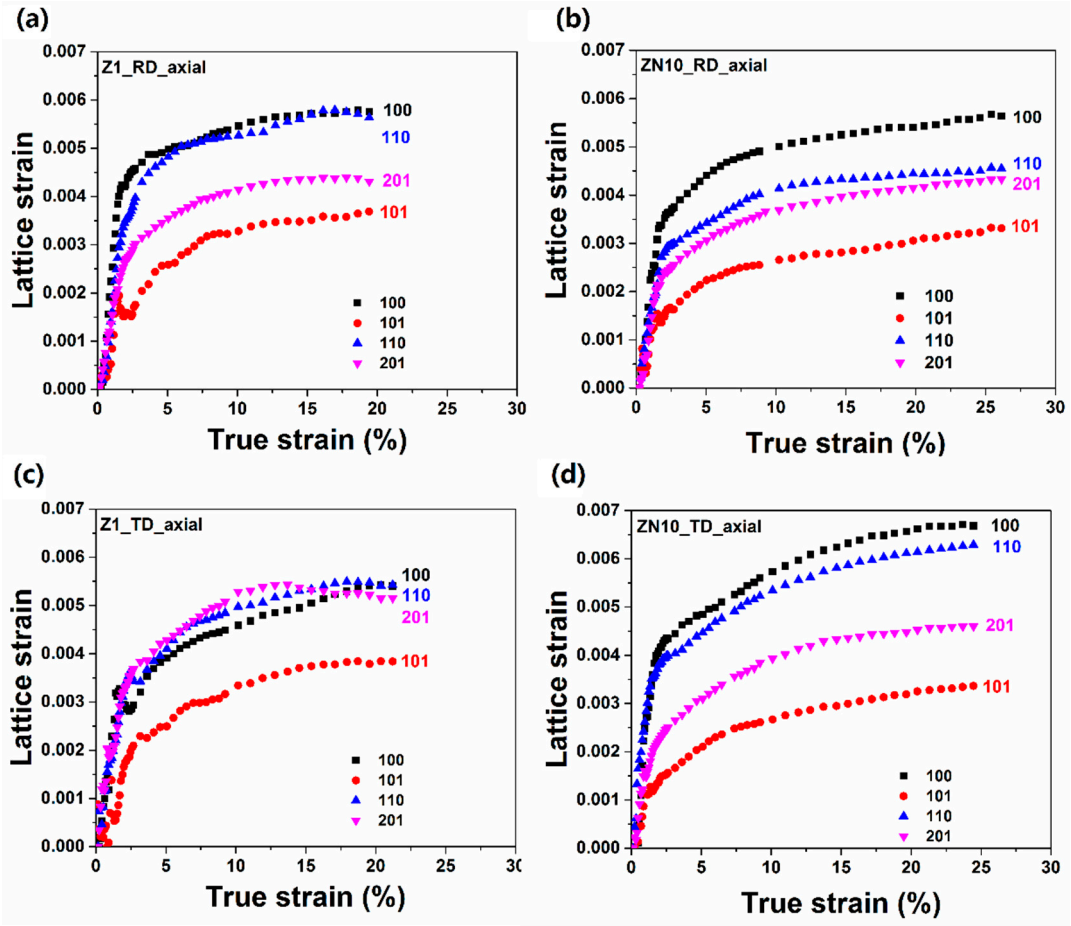

Figure 9. Lattice strain evolution of Z1 and ZN10 during tension along loading direction: (**a**) Z1 in RD; (**b**) ZN10 in RD; (**c**) Z1 in TD; (**d**) ZN10 in TD.

The true strain-lattice strain curve of {101} indicated the variation of basal slip during the deformation, while the variations of {100} and {110} planes refer to the prismatic slip. Generally, {101} plane was first deviated from the elastic linearity, showing a lowest 'yield' strain. It suggested the basal slip is the softest deformation slip in the alloys. Thus, it can be observed that the basal slip was first activated and dominant at the beginning of plastic deformation. In comparison, the {100} plane was last to deviate for all the conditions, which needed higher energy for the activity than the basal slip. This difference resulted from different CRSS for the initiation of different glide systems in the presented samples [41].

The lattice strain differences between different {hkl} lattice planes were largest in ZN10 along the TD sample in this work, which is possibly related to initial texture and the addition of the alloying element Nd. In comparison, the lattice strain of {101} grains in ZN10 was lower than in Z1 regardless of TD or RD, indicating lower active energy of basal slip for ZN10 than Z1 for the initial plastic deformation. Furthermore, in the plastic region, the differences between {100} and {110} lattice planes in ZN10 were more evident than in Z1 as shown in Figure 9.

As for the yield point, the {100} and {110} planes were larger for Z1 in RD than TD, but it was smaller for {101} plane in RD. The reasons for these differences are material anisotropy. Moreover, the {101} plane exhibited the lowest yield point of ZN10 in TD, but the highest for Z1 in RD, which agrees with the lowest yield strength of ZN10 in TD, but the highest yield strength of Z1 in RD. The yield point difference between {100} and {110} in ZN10 along RD is more pronounced compared to other samples. The reasons for these differences are the alloying elements and the initial texture (IPF of ZN10 in Figure 6) [42].

The hardening rate of lattice strain for all {hkl} planes decreased during the deformation, but the hardening rate of {100} and {110} lattice planes in ZN10 was higher than in Z1.

3.5. Modeling Results

Based on the EVPSC simulation and the experimental data, such as initial texture data, the relative deformation mode activity with texture development can be simulated. The simulation parameters for the slip and twinning modes are given in Table 2.

Table 2. Simulation parameters for deformation modes and twinning used in the simulation (unit of all shear stress values is GPa).

Alloy (Z1)	τ_0	τ_1	θ_0	θ_1
<a>—basal	0.02	0.008	0.2	0
<a>—prismatic	0.05	0.045	0.5	0
<c + a>—pyramidal 2nd order	0.09	0.08	0.8	0
Tensile twinning	0.01	0	0.2	0
Alloy (ZN10)	-	-	-	-
<a>—basal	0.02	0.008	0.2	0
<a>—prismatic	0.06	0.04	0.45	0
<c + a>—pyramidal 2nd order	0.07	0.08	0.8	0
Tensile twinning	0.04	0	0.2	0.2

The experimental (Figure 5) results of the flow stress-strain curves and the texture are in well agreement with the simulated results (Figure 10).

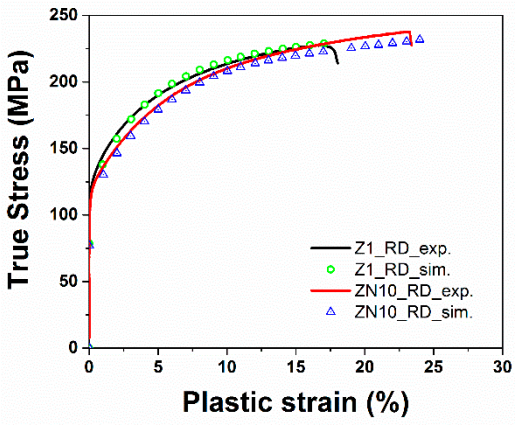

Figure 10. Experimental and simulated of true stress-plastic strain curves of Z1 and ZN10 along RD.

Figure 11 presents the simulated pole figures for both alloys at strain 20%. Comparing the texture components of experimental (Figure 7) texture and simulated texture are in well agreement, but it shows a stronger texture intensity of simulation than that in experiments.

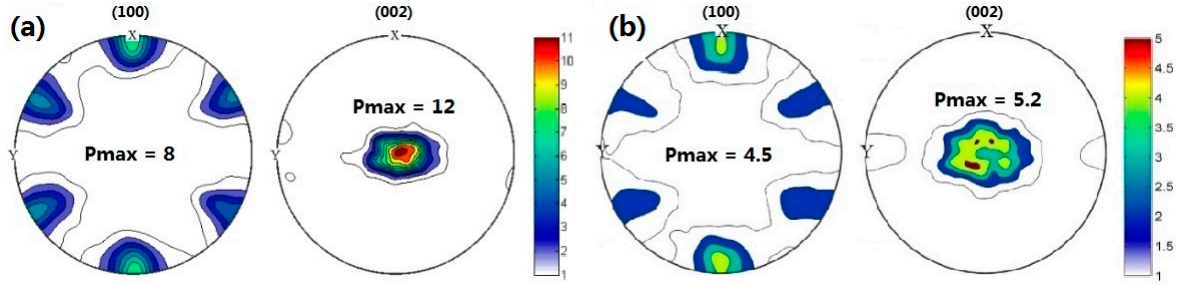

Figure 11. Simulated pole figures at 20% strain: (**a**) Z1 along RD; (**b**) ZN10 along RD.

Figure 12 presents the activity variations of the relative deformation mode as a function of the strain. The results presented two dominated deformation modes for both alloys: the increasing activity of prismatic slip and the decreasing activity of basal slip as the strain increases. The activity of those slipping results in the enhancement of the {10.0} texture component. Additionally, the twinning mode could be observed for both alloys at the initial strain stage, but slightly higher for ZN10 than Z1. The pyramidal mode could also be found for ZN10, but not for Z1, because the CRSS value of pyramidal slip in Z1 is higher than in ZN10. The activity of prismatic mode played a dominant role in the Z1 alloy deformation during all the tensile tests. However, the basal mode showed the highest activity for ZN10, but the prismatic slip turned out to be the predominant factor when the strain was less than 15%. The reasons for these differences of activity varying for Z1 and ZN10 are the alloying elements Nd and the initial crystallographic texture. Furthermore, the addition of Nd increases the CRSS value of prismatic slip [22] and decreases the CRSS value of pyramidal slip.

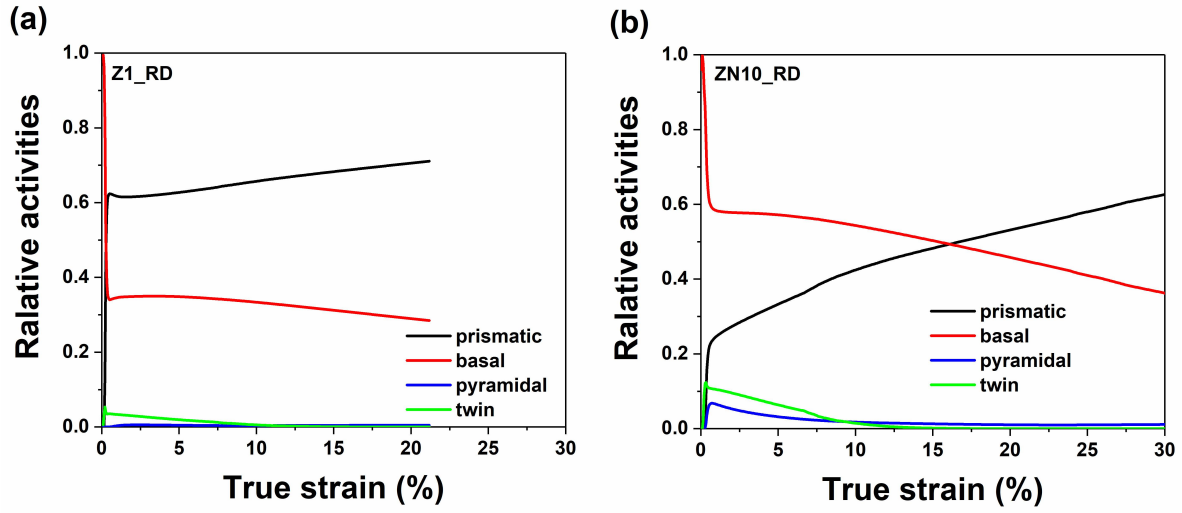

Figure 12. The relative deformation mode activities as a function of the strain: (**a**) Z1 along RD; (**b**) ZN10 along RD.

4. Discussion

4.1. Initial Texture and Texture Evolution

For the initial texture of the rolled alloys, the main components in Z1 are <00.2> fiber // ND and small fraction of <10.0> fiber // RD. The primary deformation mechanisms are basal and prismatic slip, because they produce <00.2> fiber // ND and a weak <10.0> fiber // RD [43,44]. In ZN10, it is more complex than Z1 due to the activity of different slip systems and/or twinning during the rolling. The reason for the weaker texture in ZN10 is the RE addition [8,9]. {00.2} pole shows much more broadening from ND to TD due to activity of prismatic slip. Compared to Z1, a new texture component {00.2}<10.0> was observed in ZN10, also reflected by the neat six-fold symmetry in the {10.0} pole figure from prismatic slip [43]. Another interesting texture component, {00.2} pole split from ND to RD ± 20°. It is combined with a small fraction of activity of pyramidal slip [19,45]. Furthermore, compared to the basal and prismatic slip-dominated deformation for Z1, more slip systems and twinning were activated for ZN10 during hot rolling.

According to the texture evolution, the partial <10.0> fiber // LD and {00.2}<10.0> components increased during tensile testing for Z1 due to the activation of prismatic slips and decreased the <00.2> fiber // ND which can be explained by the reduction of basal slip activation. When the tensile strain reached at 20%, the newly formed component in {00.2} plane in TD (Figure 7) was possibly formed due to the activation of tensile twinning. This component has a low intensity compared with the intensity of other texture components, suggesting that the tensile twinning plays a minor role in deformation

mechanism. In ZN10, similar increase in the partial <10.0> fiber // LD is obtained during tensile test. This component becomes a complete fiber at 10% strain, leading to the broadening ±90° of {00.2} pole from ND to TD. The reason for these variations is the activation of prismatic slip. However, the complete <002> fiber // ND changes to partial fiber for ZN10 due to the decreasing of the activation of basal glide during tensile testing. The splitting of the {00.2} pole from ND to LD is still visible throughout the deformation process, indicating the pyramidal slip is activated in the material [19,46]. Additionally, the primary deformation mechanisms for both alloys during the tensile testing are the basal and prismatic slips. A small fraction of twinning is also possibly activated in Z1, although it is the activation of pyramidal glide in the case of ZN10 rather than twinning.

4.2. Lattice Strain Evolution

In the elastic region, the lattice strains of different {hkl} lattice planes depend on elastic anisotropy and texture of the material. Due to the nearly elastic isotropy of Mg alloys compared to other material, e.g., copper or steel which have higher elastic anisotropy [47], the lattice strains for different lattice planes show a similar strain rate. After the elastic area, a fluctuation can be seen in the lattice strain curve of {10.1} plane, which is more obvious for Z1 than ZN10. The reason for this can be the activation of the twinning. This can result in the sudden rotation of gains, thereby leading to a non-gradient lattice strain curve. The curve of {10.1} plane is lower for ZN10 than Z1, it could be the reason the yield point of ZN10 is lower than Z1, i.e., ZN10 starts plastic deformation earlier than Z1 (see Table 1 and Figure 5). It is of interest to note that the difference of lattice strain curves between {10.0} and {110} in ZN10 is larger than in Z1, which could result from the initial texture, one can see clearly that ZN10 shows much higher variation between {10.0} and {11.0} in RD and TD samples (Figure 6) which indicates differences in the properties in both planes. Additionally, the presence of Nd in the material changes the volume fraction of the activation of the basal and prismatic slips during the tensile testing.

4.3. Deformation Mode Activity by EVPSC

Based on the EVPSC method, the variations of relative deformation mode activity with texture development can be simulated. The simulated results showed the primary deformation modes during tensile testing are basal and prismatic slips. The basal slip is activated easily in random material [44] during tensile testing. The activation of the basal slip decreases because of the decreased fraction of other texture components in the present alloys. At the beginning, prismatic slip is dominant in the deformation in Z1 because of the lower CRSS value of prismatic slip. The activation of the basal slip is more important to the deformation of ZN10 due to the high-volume fraction of other texture components. These simulated results are in good agreement with the experimental results. However, some differences, for example, intensity, could also be obtained by comparing the measured pole figure with the simulated pole figure. The reasons for these differences are listed as follows:

- The intensities of simulated pole figures are slightly higher than the experimental pole figures. This higher intensity could be caused by the influence of neighboring crystals on grain rotation rate. In simulation, grain-to-grain interactions on average were taken into account without neighboring effects. However, from experimental results, grain rotation is more difficult since in reality a grain is always surrounded by other grains with different orientations.
- Inhomogeneity of deformations occurs in measurements but not in simulations. In the simulation procedure the strain is homogenously accommodated by the active slip system and twinning [10].
- In simulation, the size of grains with particular orientations are homogenous. The grain size and the volume fraction of grain with certain sizes varies in the materials. Twinning is much easier formed for large grains than the small ones [46].

5. Conclusions

In the present study, the tensile deformation behaviors of Z1 and ZN10 along RD and TD were investigated using in situ synchrotron measurements and EVPSC simulation. Based on the results, the following conclusions about the effect of Nd on the deformation of Mg–Zn alloy can be obtained:

(a) The addition of Nd weakens the texture of Mg–Zn alloy, results in the formation of the {00.2}<10.0> component after hot rolling, which does not exist in the Z1 alloy. The volume fraction of this component remains stable in Nd-containing alloys, but it gradually increases with the increasing strain for Nd-free alloys.

(b) Basal slip in Nd-containing alloys are easier to active during the tensile loading compared to Nd-free alloys, it is in good agreement with the lower yield point of Nd-containing alloy.

(c) The addition of Nd increases the CRSS value of prismatic slip and decreases the CRSS value of pyramidal slip compared to Nd-free alloy.

Author Contributions: S.Y., J.B. and H.-G.B. conceived and designed the experiments; C.H. and X.Z. performed the experiments; C.H. and X.Z. analyzed the data; C.H. and X.Z. contributed materials; N.S., Y.C. and M.Z. contributed analysis tools; X.Z., Y.C. and H.-G.B. wrote the paper. All authors have read and agreed to the published version of the manuscript.

Funding: This research was funded by the German Research Foundation (DFG) grant number BO 2461/4-1, Yi 103/2-1 and BR 961/7-1, Research Start-up Funds of DGUT grant number GC300502-43 and the Academic and technical Leaders of Major Disciplines in Jiangxi Province grant number 20182BCB22020. The authors appreciate Mr Bernd. Schwebke for technical support in DESY, Junjun Shen, Xun Zeng and Ruiqing Hou for their assistance.

Conflicts of Interest: The authors declare no conflict of interest.

References

1. Friedrich, H.; Schumann, S. Forschungsstrategien für ein zweites "magnesium–zeitalter" im fahrzeugbau. *Mater. Werkst.* **2001**, *32*, 6–12. [CrossRef]
2. Kelley, E.; Hosford, W. Plane-strain compression of magnesium and magnesium alloy crystals. *Trans. Met. Soc. AIME* **1968**, *242*, 5–13.
3. Lou, X.; Li, M.; Boger, R.; Agnew, S.; Wagoner, R. Hardening evolution of az31b mg sheet. *Int. J. Plast.* **2007**, *23*, 44–86. [CrossRef]
4. Dillamore, I.; Hazel, R.; Watson, T.; Hadden, P. An experimental study of the mechanical anisotropy of some common metals. *Int. J. Mech. Sci.* **1971**, *13*, 1049–1061. [CrossRef]
5. Barnett, M.; Keshavarz, Z.; Beer, A.; Atwell, D. Influence of grain size on the compressive deformation of wrought mg–3al–1zn. *Acta Mater.* **2004**, *52*, 5093–5103. [CrossRef]
6. Yoo, M. Slip, twinning, and fracture in hexagonal close-packed metals. *Metall. Trans. A* **1981**, *12*, 409–418. [CrossRef]
7. Kelley, E. The deformation characteristics of textured magnesium. *Trans. Met. Soc. AIME* **1968**, *242*, 654–660.
8. Bohlen, J.; Nürnberg, M.R.; Senn, J.W.; Letzig, D.; Agnew, S.R. The texture and anisotropy of magnesium–zinc–rare earth alloy sheets. *Acta Mater.* **2007**, *55*, 2101–2112. [CrossRef]
9. Al-Samman, T.; Li, X. Sheet texture modification in magnesium-based alloys by selective rare earth alloying. *Mater. Sci. Eng. A* **2011**, *528*, 3809–3822. [CrossRef]
10. Barnett, M.; Nave, M.; Bettles, C. Deformation microstructures and textures of some cold rolled mg alloys. *Mater. Sci. Eng. A* **2004**, *386*, 205–211. [CrossRef]
11. Del Valle, J.; Carreño, F.; Ruano, O.A. Influence of texture and grain size on work hardening and ductility in magnesium-based alloys processed by ecap and rolling. *Acta Mater.* **2006**, *54*, 4247–4259. [CrossRef]
12. Gall, S.; Coelho, R.; Müller, S.; Reimers, W. Mechanical properties and forming behavior of extruded az31 and me21 magnesium alloy sheets. *Mater. Sci. Eng. A* **2013**, *579*, 180–187. [CrossRef]
13. Dobroň, P.; Chmelík, F.; Yi, S.; Parfenenko, K.; Letzig, D.; Bohlen, J. Grain size effects on deformation twinning in an extruded magnesium alloy tested in compression. *Scr. Mater.* **2011**, *65*, 424–427. [CrossRef]
14. Barnett, M. A rationale for the strong dependence of mechanical twinning on grain size. *Scr. Mater.* **2008**, *59*, 696–698. [CrossRef]

15. Agnew, S.; Mulay, R.; Polesak Iii, F.; Calhoun, C.; Bhattacharyya, J.; Clausen, B. In situ neutron diffraction and polycrystal plasticity modeling of a mg–y–nd–zr alloy: Effects of precipitation on individual deformation mechanisms. *Acta Mater.* **2013**, *61*, 3769–3780. [CrossRef]
16. Stanford, N.; Geng, J.; Chun, Y.; Davies, C.; Nie, J.; Barnett, M. Effect of plate-shaped particle distributions on the deformation behaviour of magnesium alloy az91 in tension and compression. *Acta Mater.* **2012**, *60*, 218–228. [CrossRef]
17. Robson, J.; Stanford, N.; Barnett, M. Effect of precipitate shape on slip and twinning in magnesium alloys. *Acta Mater.* **2011**, *59*, 1945–1956. [CrossRef]
18. Lentz, M.; Klaus, M.; Wagner, M.; Fahrenson, C.; Beyerlein, I.J.; Zecevic, M.; Reimers, W.; Knezevic, M. Effect of age hardening on the deformation behavior of an mg–y–nd alloy: In-situ x-ray diffraction and crystal plasticity modeling. *Mater. Sci. Eng. A* **2015**, *628*, 396–409. [CrossRef]
19. Agnew, S.; Yoo, M.; Tome, C. Application of texture simulation to understanding mechanical behavior of mg and solid solution alloys containing li or y. *Acta Mater.* **2001**, *49*, 4277–4289. [CrossRef]
20. Stanford, N.; Cottam, R.; Davis, B.; Robson, J. Evaluating the effect of yttrium as a solute strengthener in magnesium using in situ neutron diffraction. *Acta Mater.* **2014**, *78*, 1–13. [CrossRef]
21. Sandlöbes, S.; Friák, M.; Zaefferer, S.; Dick, A.; Yi, S.; Letzig, D.; Pei, Z.; Zhu, L.-F.; Neugebauer, J.; Raabe, D. The relation between ductility and stacking fault energies in mg and mg–y alloys. *Acta Mater.* **2012**, *60*, 3011–3021. [CrossRef]
22. Herrera-Solaz, V.; Hidalgo-Manrique, P.; Pérez-Prado, M.T.; Letzig, D.; Llorca, J.; Segurado, J. Effect of rare earth additions on the critical resolved shear stresses of magnesium alloys. *Mater. Lett.* **2014**, *128*, 199–203. [CrossRef]
23. Zhang, Q.; Fan, T.-W.; Fu, L.; Tang, B.-Y.; Peng, L.-M.; Ding, W.-J. Ab-initio study of the effect of rare-earth elements on the stacking faults of mg solid solutions. *Intermetallics* **2012**, *29*, 21–26. [CrossRef]
24. Ha, C.; Bohlen, J.; Yi, S.; Zhou, X.; Brokmeier, H.-G.; Schell, N.; Letzig, D.; Kainer, K.U. Influence of nd or ca addition on the dislocation activity and texture changes of mg–zn alloy sheets under uniaxial tensile loading. *Mater. Sci. Eng. A* **2019**, *761*, 138053. [CrossRef]
25. Peng, Q.; Li, X.; Ma, N.; Liu, R.; Zhang, H. Effects of backward extrusion on mechanical and degradation properties of mg–zn biomaterial. *J. Mech. Behav. Biomed. Mater.* **2012**, *10*, 128–137. [CrossRef] [PubMed]
26. Ha, C.; Yi, S.; Bohlen, J.; Zhou, X.; Brokmeier, H.-G.; Schell, N.; Letzig, D.; Kainer, K.U. Deformation and recrystallization mechanisms and their influence on the microstructure development of rare earth containing magnesium sheets. In Proceedings of the TMS Annual Meeting & Exhibition, Phoenix, AZ, USA, 11–15 March 2018; Springer: Berlin, Germany; pp. 209–216.
27. Kree, V.; Bohlen, J.; Letzig, D.; Kainer, K.U. Metallographische gefügeuntersuchungen von magnesium-legierungen. *Prakt. Metallogr.* **2004**, *41*, 233–246.
28. Brokmeier, H.G. Hot rectangular extrusion textures of six mg-alloys via neutron diffraction. *Adv. Eng. Mater.* **2018**, *20*, 1700234. [CrossRef]
29. Bachmann, F.; Hielscher, R.; Schaeben, H. *Texture Analysis with Mtex–Free and Open Source Software Toolbox*; Klein, H., Schwarzer, R.A., Eds.; Trans Tech Publications: Baech, Switzerland, 2010; pp. 63–68.
30. Molinari, A.; Canova, G.; Ahzi, S. A self consistent approach of the large deformation polycrystal viscoplasticity. *Acta Metall.* **1987**, *35*, 2983–2994. [CrossRef]
31. Wang, H.; Wu, P.; Tomé, C.; Huang, Y. A finite strain elastic–viscoplastic self-consistent model for polycrystalline materials. *J. Mech. Phys. Solids* **2010**, *58*, 594–612. [CrossRef]
32. Chi, Y.; Zhou, X.; Xu, C.; Sun, D.; Qiao, X.; Brokmeier, H.; Zheng, M. The origin of discontinuous yielding in mg alloys under slip-dominated condition studied by in-situ synchrotron diffraction and elastic-viscoplastic self-consistent modeling. *Mater. Sci. Eng. A* **2019**, *754*, 562–568. [CrossRef]
33. Tomé, C.; Lebensohn, R.A.; Kocks, U. A model for texture development dominated by deformation twinning: Application to zirconium alloys. *Acta Metall. Mater.* **1991**, *39*, 2667–2680. [CrossRef]
34. Lebensohn, R.A.; Tomé, C. A self-consistent anisotropic approach for the simulation of plastic deformation and texture development of polycrystals: Application to zirconium alloys. *Acta Metall. Mater.* **1993**, *41*, 2611–2624. [CrossRef]
35. Turner, P.; Tomé, C. A study of residual stresses in zircaloy-2 with rod texture. *Acta Metall. Mater.* **1994**, *42*, 4143–4153. [CrossRef]

36. Tomé, C.N. Self-consistent polycrystal models: A directional compliance criterion to describe grain interactions. *Model. Simul. Mater. Sci. Eng.* **1999**, *7*, 723. [CrossRef]
37. Agnew, S.; Mehrotra, P.; Lillo, T.; Stoica, G.; Liaw, P. Texture evolution of five wrought magnesium alloys during route a equal channel angular extrusion: Experiments and simulations. *Acta Mater.* **2005**, *53*, 3135–3146. [CrossRef]
38. Agnew, S.R.; Duygulu, Ö. Plastic anisotropy and the role of non-basal slip in magnesium alloy az31b. *Int. J. Plast.* **2005**, *21*, 1161–1193. [CrossRef]
39. Wang, H.; Wu, P.; Wang, J.; Tomé, C. A crystal plasticity model for hexagonal close packed (hcp) crystals including twinning and de-twinning mechanisms. *Int. J. Plast.* **2013**, *49*, 36–52. [CrossRef]
40. Asaro, R.J.; Needleman, A. Overview no. 42 texture development and strain hardening in rate dependent polycrystals. *Acta Metall.* **1985**, *33*, 923–953. [CrossRef]
41. Schmid, E. Yield Point of Crystals, Critical Shear Stress Law. In Proceedings of the First International Congress for Applied Mechanics, Delft, The Netherland, 22–26 April 1924.
42. Kamaya, M. A procedure for estimating young's modulus of textured polycrystalline materials. *Int. J. Solids Struct.* **2009**, *46*, 2642–2649. [CrossRef]
43. Agnew, S. Plastic anisotropy of magnesium alloy az31b sheet. In *Essential Readings in Magnesium Technology*; Springer: Berlin, Germany, 2016; pp. 351–356.
44. Steiner, M.; Bhattacharyya, J.; Agnew, S. The origin and enhancement of {0001}< 112¯ 0> texture during heat treatment of rolled az31b magnesium alloys. *Acta Materialia* **2015**, *95*, 443–455.
45. Styczynski, A.; Hartig, C.; Bohlen, J.; Letzig, D. Cold rolling textures in az31 wrought magnesium alloy. *Scr. Mater.* **2004**, *50*, 943–947. [CrossRef]
46. Yi, S.-B.; Davies, C.; Brokmeier, H.-G.; Bolmaro, R.; Kainer, K.; Homeyer, J. Deformation and texture evolution in az31 magnesium alloy during uniaxial loading. *Acta Mater.* **2006**, *54*, 549–562. [CrossRef]
47. Clausen, B.; Lorentzen, T.; Leffers, T. Self-consistent modelling of the plastic deformation of fcc polycrystals and its implications for diffraction measurements of internal stresses. *Acta Mater.* **1998**, *46*, 3087–3098. [CrossRef]